Nanoscale Horizons

ROYAL SOCIETY OF CHEMISTRY

COMMUNICATION

View Article Online
View Journal | View Issue

Cite this: *Nanoscale Horiz.*, 2026, **11**, 488

Received 28th September 2025,
Accepted 6th November 2025

DOI: 10.1039/d5nh00662g

rsc.li/nanoscale-horizons

Complementary chemical adsorption of iodine species on MXene/carboxylated CNTs for high loading zinc–iodine batteries

Aidi Fu, Guohao Li, Yingxinjie Wang, Jie Wang, Jiale Fan, Jiamin Liu, Nan Zhang and Xiuqiang Xie *

Zinc–iodine rechargeable batteries offer inherent safety and abundant reserves, making them promising for energy storage applications. However, the poor interfacial stability of the zinc anode and the shuttle effect, both caused by the diffusion of soluble polyiodides in aqueous media, significantly compromise device stability, especially at high mass loadings. This work proposes a complementary chemical adsorption strategy to achieve high-loading zinc–iodine batteries, utilizing a composite material of $Ti_3C_2T_x$ MXene and carboxylated multi-walled carbon nanotubes (c-MCNTs) as an iodine carrier. Carboxylated multi-walled carbon nanotubes (c-MCNTs) form C–I bonds with initial I^- ions through chemical interactions, while $Ti_3C_2T_x$ MXene effectively chemically adsorbs the byproduct I_3^- ions formed during charging and discharging, enabling the adsorption of a substantial amount of iodine species. Therefore, even at a high areal mass loading of 33.27 mg cm^{-2}, the prepared zinc–iodine battery delivers a high areal capacity of 2.82 mAh cm^{-2} at a current density of 5 mA cm^{-2}, surpassing most previously reported zinc–iodine batteries, while maintaining excellent cycling stability with a capacity retention of 99.04% after 300 cycles. Moreover, it exhibits outstanding rate performance, retaining an areal capacity of 1.52 mAh cm^{-2} even at a high current density of 50 mA cm^{-2}. This strategy is also potentially extendable to the design of other high-loading metal–iodine batteries.

New concepts

In this study, we propose a novel strategy to achieve high loading zinc–iodine batteries by preparing a composite material of MXene and carboxylated CNTs. This composite is used as a host to immobilize iodine species and suppress the shuttle effect. Unlike conventional physical adsorption or single-mode chemical adsorption, our strategy leverages the complementary chemical adsorption of the two materials. Specifically, MXene can efficiently chemically adsorb the generated I_3^- ions during charge–discharge, while carboxylated CNTs can chemically adsorb the initial I^- ions. This design, which can simultaneously immobilize the iodine source and polyiodide species, significantly enhances the active material loading and areal capacity. This work provides a promising approach for other high loading metal–iodine batteries.

1. Introduction

In recent decades, aqueous zinc-based batteries have been extensively studied as a promising candidate for electrochemical energy storage. This is ascribed to the high theoretical specific capacity (820 mAh g^{-1}), abundant resource availability, low electrode potential relative to the standard hydrogen electrode (SHE) (−0.76 V), and excellent air stability of Zn.[1–3] Iodine (I_2) has low solubility in water (≈0.29 g L^{-1}),[4] making it suitable for aqueous batteries. Different from traditional zinc batteries that typically rely on the insertion and extraction of Zn^{2+} ions, aqueous zinc–iodine (Zn–I_2) batteries store energy based on the iodine redox reaction at the cathode and zinc deposition/stripping at the anode. The implementation of iodine redox electrochemistry in aqueous zinc-based batteries delivers a considerable voltage and a high theoretical capacity of 211 mAh g^{-1}, attracting extensive research attention.[5,6] Despite these advantages and significant recent breakthroughs, the development of zinc–iodine batteries remains in its early stages, especially for the commercialization at high mass loadings due to several critical challenges. First, iodine has poor conductivity and is unstable, which requires a host material. Second, during redox reactions, iodine readily forms soluble polyiodide intermediates. This leads to a shuttle effect, causing active material loss, thereby reducing coulombic efficiency and cycle stability.[7,8] Third, the kinetics of iodine conversion are slow, promoting polyiodide accumulation in the electrolyte. This further exacerbates the shuttle effect and hinders the development of high-loading iodine cathodes.[9,10] Additionally, the stability of the zinc anode is compromised by the

College of Materials Science and Engineering, Hunan University, Changsha, 410082, P. R. China. E-mail: xiuqiang_xie@hnu.edu.cn

polyiodide shuttle effect due to the corrosion reaction between polyiodides and zinc.[11,12] The exploration of an appropriate host material remains a research hotspot in zinc–iodine batteries.[13]

The primary strategies for mitigating the shuttle effect in zinc–iodine batteries involve the development of iodine host materials.[14] Previous studies have demonstrated that the nanopores and high specific surface area of porous carbon materials serve as excellent reservoirs for encapsulating iodine and polyiodide species. For example, Pan *et al.* have employed microporous activated carbon fiber fabric (ACF) to load iodine-active materials *via* a simple adsorption method, confirming that carbon nanopores effectively adsorb polyiodides and suppress the shuttle effect.[15] Beyond conventional physical confinement, optimizing carbon matrices with chemical adsorption functionality represents a highly promising approach for stabilizing iodine and preventing polyiodide dissolution/shuttling. For instance, Ye *et al.* have constructed a zeolite-imidazolate framework (ZIF)-derived carbon matrix combining Ni/Zn bimetallic anchoring with nitrogen self-doping.[16] Abundant heteroatom doping and customized unsaturated coordination environments establish multiple strong chemical adsorption sites, synergistically inhibiting polyiodide migration. Progress in carbon material design has inspired further exploration of conductive hosts with spatially constrained structures and adsorption sites. Notable examples include Prussian blue analogues (PBAs),[17] MXenes,[18–20] and metal–organic frameworks (MOFs).[21] Zhao *et al.* have utilized 2D layered Nb_2CT_x MXene—which exhibits high conductivity, abundant surface functional groups (=O, –F, and –OH), and a periodically arranged interlayer structure—as an iodine host.[13] This material effectively fixes iodine/polyiodides between layers through complementary physical confinement and chemical adsorption, thereby suppressing shuttle effects. However, these iodine hosts have primarily been applied under low-loading conditions. Enhancing performance under high-loading remains a significant challenge. First, increased iodine content at high loadings leads to a higher concentration of polyiodide species, which exacerbates the shuttle effect. Second, high loading typically results in thicker electrode layers, extending ion diffusion pathways and thus hindering ion transport, which slows down reaction kinetics. Third, the uneven distribution of active iodine species in thick electrodes can lead to incomplete utilization, with some active material remaining electrochemically inaccessible, ultimately reducing the overall capacity.

Here, we propose a complementary chemical adsorption strategy to achieve high loading in zinc–iodine batteries, using a composite material of $Ti_3C_2T_x$ MXene and carboxylated multi-walled carbon nanotubes (c-MCNTs) as an iodine carrier. MXene exhibits high conductivity and abundant surface functional groups, enabling effective chemical adsorption of polyiodides.[22] On the other hand, c-MCNTs serve as a structurally stable conductive framework, capable of forming bonds with iodine ions, thus chemically adsorbing iodine sources.[23] These two components adsorb different iodine species, resulting in complementary chemical adsorption. Additionally, the composite material formed demonstrates a hierarchical porous structure, which physically restricts the leakage of iodine species and fosters ion transport, thereby achieving high iodine loading. To explore the performance of zinc–iodine batteries under high loading conditions, zinc iodide solution is used as the iodine source and added to the carrier material, resulting in the fabrication of high-performance electrodes based on the MC composite. At a high loading of 33.27 mg cm^{-2}, the prepared zinc–iodine battery delivers a high areal capacity of 2.82 mAh cm^{-2} at 5 mA cm^{-2}. Additionally, after 300 cycles, it retains 99.04% of its capacity. The battery also demonstrates excellent rate performance, maintaining an areal capacity of 1.52 mAh cm^{-2} even at a current density of 50 mA cm^{-2}. The promise is exemplified by assembling a pouch cell, which delivers an areal capacity of 3.71 mAh cm^{-2} at a current density of 15 mA cm^{-2}. This strategy addresses several challenges associated with high loading, effectively suppressing the shuttle effect and enhancing ion transport to achieve high areal capacity.

2. Results and discussion

Fig. 1 shows a schematic diagram of the manufacturing process for $Ti_3C_2T_x$ MXene and c-MCNT composite cathodes. This process involves freeze-drying the mixed electrode slurry, followed by coating and iodine loading (cathode permeation) process. The slurry, which contains $Ti_3C_2T_x$ MXene nanosheets and carboxylated multi-walled carbon nanotubes (c-MCNTs), is coated onto a carbon fabric. ZnI_2 solution serves as the iodine source, with iodine fully diffused into the carrier in the form of iodine ions, resulting in the composite cathode MXene-CNT-I (denoted as MC-I^-). For comparison, MXene and c-MCNTs are prepared using similar manufacturing processes.

$Ti_3C_2T_x$ MXene nanosheets are etched and exfoliated from Ti_3AlC_2 (Fig. S1), and the scanning electron microscopy (SEM) micrographs of $Ti_3C_2T_x$ MXene and c-MCNTs are shown in Fig. 2a and Fig. S2. These two components have different chemical adsorption interactions. Fig. 2b illustrates the top-view scanning electron microscopy (SEM) micrograph of the MC composite electrode, which reveals that c-MCNTs uniformly wrap around the MXene nanosheets and forms a porous electrode. Fig. 2c presents the top-view SEM image of the high-loading MC-I^- cathode, accompanied by corresponding

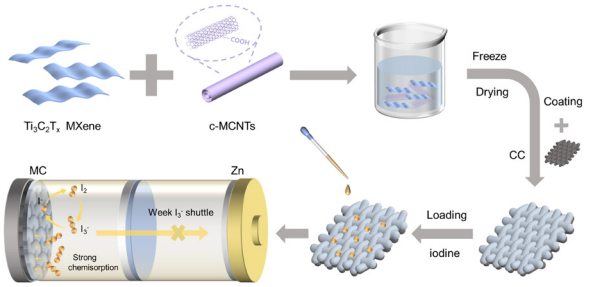

Fig. 1 Schematic illustration showing the preparation process and the unique advantages of the high iodine-loaded MC-I^- cathode.

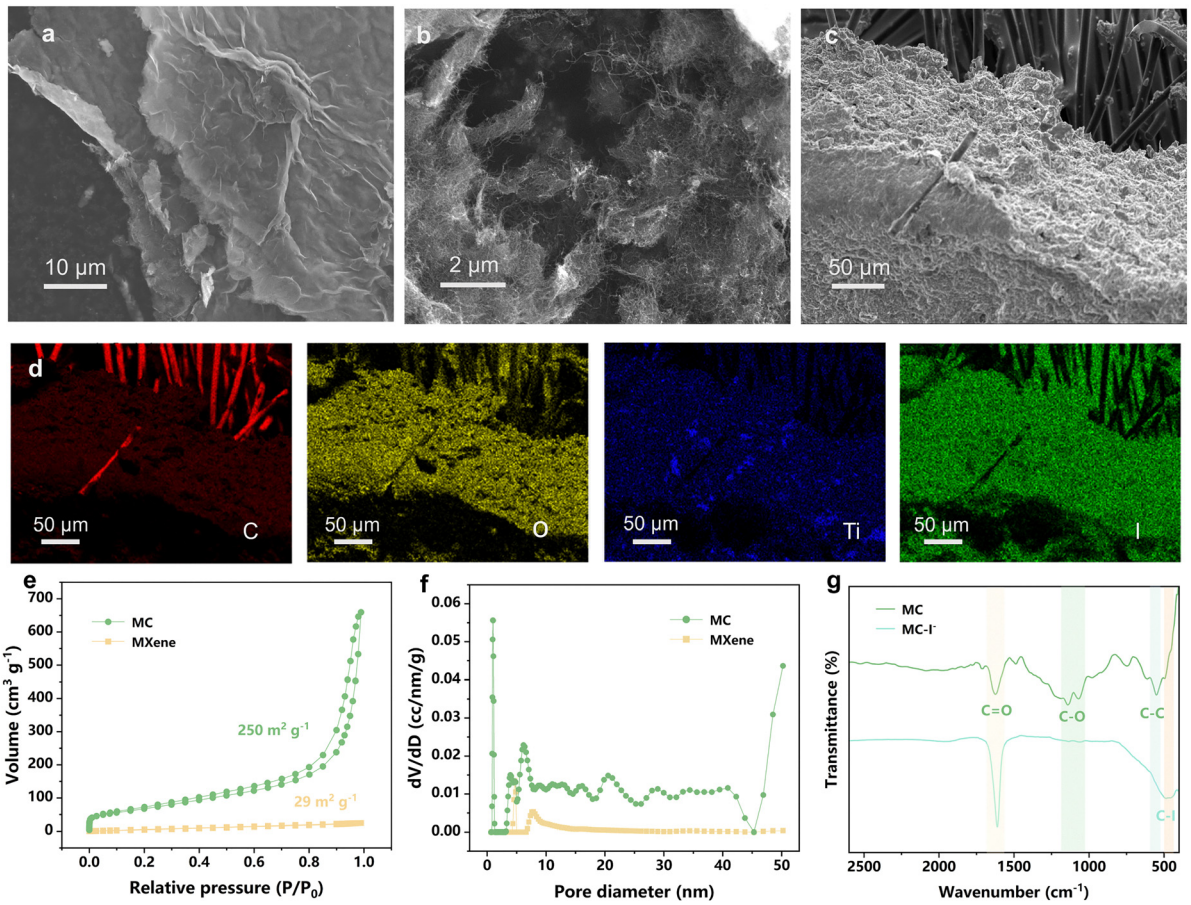

Fig. 2 Morphological and structural characterization of MC electrodes. (a) and (b) Top-view SEM images of the MXene electrode and the MC electrode. (c) and (d) Top-view SEM image and the corresponding C, O, Ti, I elemental mapping images of the MC-I^- cathode after loading iodine. (e) and (f) Specific surface area and the corresponding pore size distribution of N_2 adsorption–desorption isotherms. (g) FTIR spectra before and after iodine plating.

elemental mapping images (Fig. 2d). The C, O, Ti, and I elemental mapping diagrams confirm the successful loading of iodine. X-ray diffraction (XRD) patterns are analyzed to reveal the evolution of phase composition. As shown in Fig. S3, a peak at $2\theta = 39^\circ$, corresponding to the (104) plane of the Ti_3AlC_2 (MAX) phase, disappears, indicating the removal of the aluminum layer.[24] The (002) peak of $Ti_3C_2T_x$ shifts from 6.9° in pure MXene to 6.2° in the composite material MC, indicating an increase in interlayer spacing. This change suggests that the interlayer structure of $Ti_3C_2T_x$ is related to the intercalation of substances during the composite process. The broad characteristic peak at 24.9° corresponds to c-MCNTs,[25] confirming their presence and contribution to the composite material. After iodine adsorption, the (002) diffraction peak of $Ti_3C_2T_x$ further shifts to a lower angle at 5.7°, indicating an increase in interlayer spacing.[13] This can be attributed to the bonding of Ti atoms in $Ti_3C_2T_x$ with iodine,[26] which facilitates the effective insertion of iodine ions into the interlayer structure, leading to an expansion of the interlayer spacing and a further shift of the (002) diffraction peak to lower angles, reflecting additional structural changes.[27] Additionally, Fig. S4 displays the Raman spectrum, featuring two broad peaks at 1358 and 1588 cm^{-1} in the MC, which correspond to the D and G bands of carbon nanotubes,[28] respectively. For the resulting MC-I^- cathode, new peaks emerge at 122 and 170 cm^{-1}, which suggests the successful introduction of iodine ions.[29] This result aligns with the findings from XRD, demonstrating that the insertion of iodine ions has an impact on the crystal structure of the composite material.

Fig. 2e presents the N_2 adsorption–desorption isotherms of the MC composite electrode and MXene. The specific surface area of the MC composite electrode (250 $m^2 g^{-1}$) is significantly higher than that of the MXene electrode (29 $m^2 g^{-1}$), suggesting a stronger adsorption capacity. The pore size distribution curve (Fig. 2f) shows that the pore size distribution of the MXene electrode is in the mesoporous region. After the addition of c-MCNTs, the MC composite electrode exhibits a hierarchical porous structure with micropores, mesopores, and macropores, which is beneficial for iodine adsorption and Zn^{2+} diffusion,[30–32] making it an ideal carrier for loading iodine-based materials. Moreover, contact angle tests show that the MC composite electrode has a low contact angle and exhibits good aqueous electrolyte-wetting behavior (Fig. S5). Compared with the large contact angles of the MXene and c-MCNT electrodes (Fig. S6), electrolyte droplets added to the surface of the MC composite electrode quickly penetrate until the

contact angle approaches zero. This property improves electrolyte infiltration and accelerates ion transport. The high specific surface area and the favorable electrolyte wetting properties of the electrode facilitate high iodine mass loading.

Then, the functional groups of MC and MC-I^- are revealed by Fourier transform infrared (FTIR) spectroscopy (Fig. 2g). Specifically, in the MC sample, a distinct characteristic absorption peak was observed around 1136 cm^{-1}, which can be attributed to the C–O stretching vibration of the carboxyl group (–COOH) on the carboxylated multi-walled carbon nanotubes.[33,34] After iodine treatment, the MC-I^- sample showed a strong new absorption peak around 491 cm^{-1}. This peak corresponds to the stretching vibration of the C–I bond,[35] indicating that iodine atoms have replaced the carboxyl group and chemically bonded with the carbon atoms of the nanotubes, forming C–I covalent bonds (Fig. S7). The appearance of this C–I peak suggests that iodine is not merely physically adsorbed onto the surface of the carbon nanotubes but is chemically integrated into the nanotube network, resulting in significant chemical adsorption.[36] Given the high iodine loading and its stable chemical bonding with the nanotube structure, this process is beneficial for the preparation of high-iodine-loaded electrodes. This structure not only enhances the electronic coupling between iodine and the conductive carbon framework but also improves the dispersion and reactivity of iodine within the electrode, thereby enhancing the overall electrochemical performance of the electrode.[23]

A series of analytical techniques are systematically employed to investigate the adsorption capacity and mechanism of MC composite materials toward iodine. Fig. 3a illustrates the visualization of the adsorption experiment of polyiodides by MC and c-MCNT adsorbents. The initial cathode electrolyte solution containing polyiodides is dark brown in color. Equal weights of MC and c-MCNTs adsorbents are introduced into two separate glass bottles, each containing 6 mL of the iodine cathode solution, and the samples are allowed to stand for 24

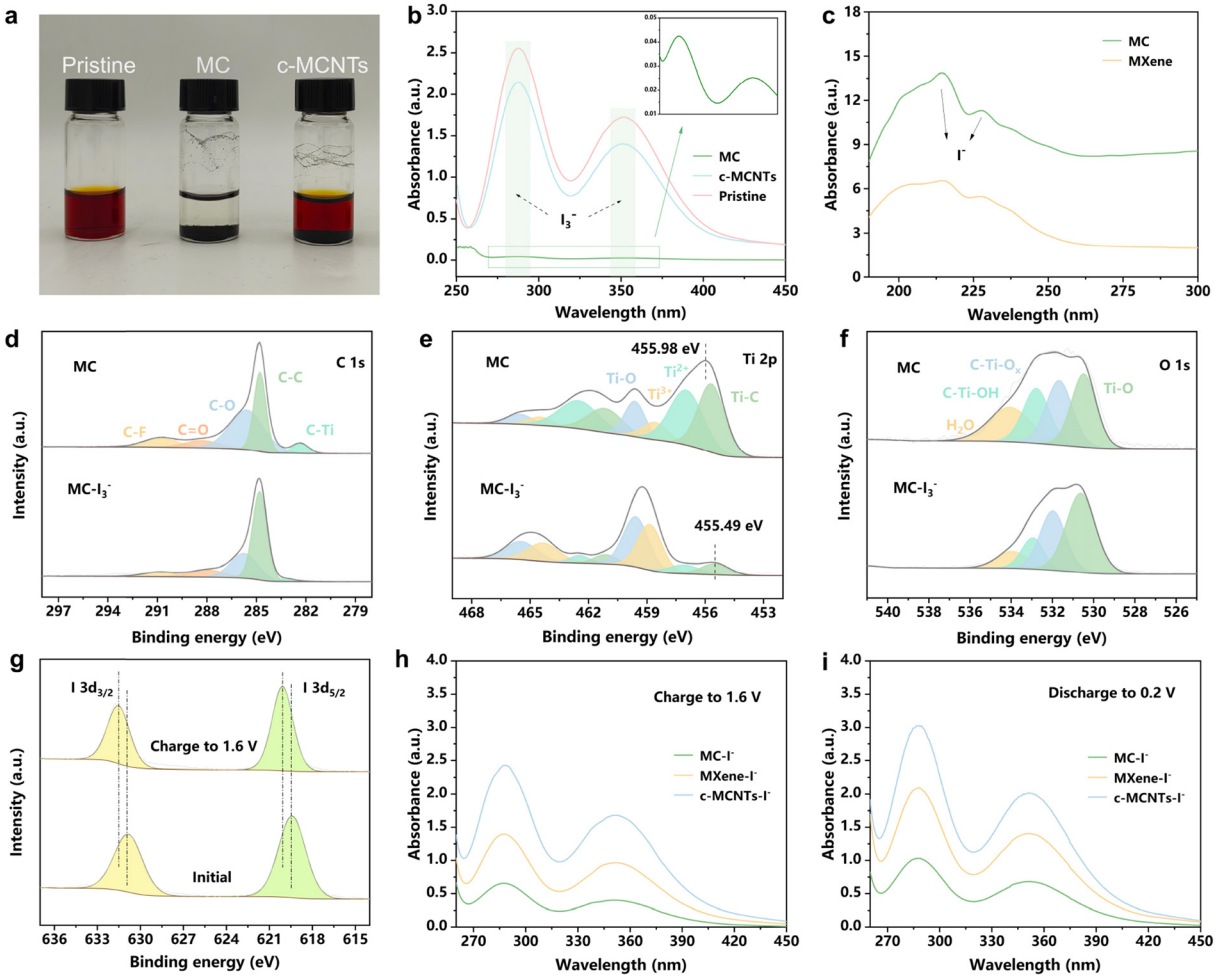

Fig. 3 Adsorption mechanism study of the MXene and c-MCNT composites for iodine species. (a) and (b) Visualization adsorption experiment and the corresponding UV-vis absorption spectra of the 16.7 mM pristine I_3^- solution, and the I catholyte solution treated with the c-MCNTs and MC adsorbents for 24 h. (c) UV-visible diffuse reflectance absorption spectra of MXene and MC adsorbents after adsorption of 2 M I^- solution for 24 hours. (d)–(f) High-resolution C 1s, Ti 2p and O 1s XPS signals of the original MC sample and the MC-I_3^- sample after adsorption of I_3^-. (g) Detailed I 3d XPS spectra of the MC-I^- cathode at different states. (h) and (i) UV-vis spectra of the electrolytes from the MC-I^-, MXene-I^-, and c-MCNTs-I^- cathodes after charging to 1.6 V and discharging to 0.2 V.

hours. As depicted in Fig. 3a, the solution with the c-MCNT adsorbent shows negligible color change, while the solution with the MC adsorbent becomes nearly transparent, indicating the high adsorption capacity of MC for polyiodides.[37] The adsorption capacities of the two adsorbents for I_3^- are investigated through UV-visible absorption measurements. As shown in Fig. 3b, the original cathode solution exhibits two strong absorption peaks at 288 and 352 nm, respectively, which are characteristic absorption signals of I_3^- species.[38,39] After treatment with MC and c-MCNT adsorbents, the I_3^- signals in the UV-visible absorption spectra decrease compared to those in the original solution samples. Notably, the peak intensity of the MC-treated samples is significantly lower than that of the c-MCNT-treated samples (inset in Fig. 3b), consistent with the visualization experiment results. This suggests that the incorporation of MXene in the composite electrode enhances the adsorption of polyiodides.

FTIR analysis indicates that c-MCNTs can form chemical bonds with iodide ions (I^-), thereby facilitating their adsorption (Fig. 2g). To demonstrate their role in the composite materials and quantify I^- adsorption capacity,[40] MC and MXene powders are immersed in a 2 M I^- solution for 24 hours, then perform ultraviolet-visible diffuse reflectance absorption measurements on the powder that has adsorbed I^-. Fig. 3c shows the adsorption of iodide ions by both MC and MXene. In the same iodide ion solution, the adsorption capacity of the MC composite material for I^- is more than twice that of MXene, indicating that the inclusion of c-MCNTs in the composite electrodes enhances the adsorption of iodide ions, which serve as the iodine source in this study.

X-ray photoelectron spectroscopy (XPS) analysis reveals changes in the chemical state of the MC composite material before and after iodine adsorption. Signals for C, Ti, O, and F are detected in both the original MC sample and the MC-I^- cathode sample (Fig. S8). However, the I signal is only detected in MC-I^-. In the I 3d high-resolution spectrum (Fig. 3g), the initial MC-I^- cathode sample exhibits distinct iodine signals at 630.84 and 619.41 eV, indicating successful adsorption of iodine species onto the MC composite material. Upon charging to 1.6 V, the I $3d_{3/2}$ and I $3d_{5/2}$ peaks shift to 631.52 and 620.06 eV, respectively.[41] The significant shift of the characteristic peaks toward higher binding energies indicates that the iodine species undergo oxidation. Fig. 3d presents the high-resolution C 1s XPS signals before and after I_3^- adsorption, showing a reduction in C–O bonds upon adsorption. This reduction suggests that some I_3^- is reduced to I^-, forming chemical bonds with carboxyl groups, thereby decreasing the C–O content. Fig. 3e displays the high-resolution Ti 2p XPS signals, where post-adsorption shifts from 455.98 eV to 455.49 eV indicate strong chemical interaction between iodine and $Ti_3C_2T_x$, altering the electronic structure and bonding environment of the Ti atoms.[22,42] Additionally, the high-resolution O 1s spectra (Fig. 3f) show a significant weakening of the Ti–OH bonding signal in the original MC sample following I_3^- adsorption. This change is mainly attributed to competitive bonding between iodine and Ti atoms, weakening the original Ti–OH bonds.[43] The larger size of the iodine species may also exert a greater steric effect on the surrounding coordination environment, further influencing the surface rearrangement of hydroxyl groups and weakening the Ti–OH bonds.[22] These results confirm that Ti metal atoms are active sites for chemical binding between MXene and I_3^-, while carboxyl groups serve as active sites for the chemical bonding between c-MCNTs and I^-.

As mentioned in the Introduction section, the shuttle effect of polyiodide intermediates leads to decreased battery capacity and cycle life. This significant challenge hinders the application of aqueous Zn–I_2 batteries, particularly those designed for practical application with high iodine active mass loading. To verify the effectiveness of the MC composite material in immobilizing polyiodides (I_3^-) during charge and discharge, a Zn–I_2 battery with an optical cuvette is subjected to UV-visible spectroscopy characterization. The iodine-loaded composite cathode (MC-I^-, MXene-I^-, or c-MCNTs-I^-) and the Zn metal anode are placed at opposite ends of the cuvette battery, using 2 M $ZnSO_4$ as the electrolyte. The cathode and anode of the cuvette battery are connected to an electrochemical workstation for charging and discharging. At charged (1.6 V) and discharged (0.2 V) states, the cuvette is placed in a UV-visible spectrometer to analyze the concentration of I_3^- polyiodides in the electrolyte.[44] As shown in Fig. 3h and i, the cuvette cells with MXene-I^- and c-MCNTs-I^- cathodes exhibit significantly higher absorbance at 288 nm and 352 nm, indicating a rapid increase in I_3^- concentration in the electrolyte during charging to 1.6 V and discharging to 0.2 V. When I^- ions are oxidized to I_2 at the cathode, they spontaneously react with I^- ions to form I_3^- intermediates ($2I^- - 2e^- \rightarrow I_2$; $I_2 + I^- \rightarrow I_3^-$),[45] which are easily dissolved in the electrolyte, resulting in high absorption peaks for I_3^- during UV-visible spectroscopy. In contrast, for the MC-I^- cathode, the I_3^- peak intensity remains at a lower level after charging and discharging, confirming the effectiveness of the MC composite in immobilizing soluble I_3^- intermediates during the charge–discharge cycle.

The electrochemical performance of most reported aqueous zinc–iodine batteries is evaluated under low iodine active material mass-loading conditions (<5 mg cm^{-2}).[14] However, for the practical application of these batteries, evaluation under high iodine loading conditions is essential. To investigate the redox activity of the MC-I^- cathode in an aqueous electrolyte, a coin-type battery is assembled using a zinc metal plate as the anode and a 2 M $ZnSO_4$ solution as the electrolyte. The redox kinetics of Zn-I_2 batteries with different cathodes (MC-I^-, MXene-I^-, and c-MCNTs-I^- with a high iodine loading of 33.27 mg cm^{-2}) are investigated using cyclic voltammetry (CV) and electrochemical impedance spectroscopy (EIS).

Fig. 4a shows the cyclic voltammetry (CV) spectra of the three cathodes at a scan rate of 1 mV s^{-1} within the voltage range of 0.2–1.6 V. All three batteries exhibit a pair of redox peaks, indicating the I_2/I^- redox reaction. Compared with MXene-I^- and c-MCNTs-I^-, MC-I^- exhibits clearer redox peaks and a higher peak current density. Additionally, the polarization overvoltage of the MC-I^- battery is lower than that of the

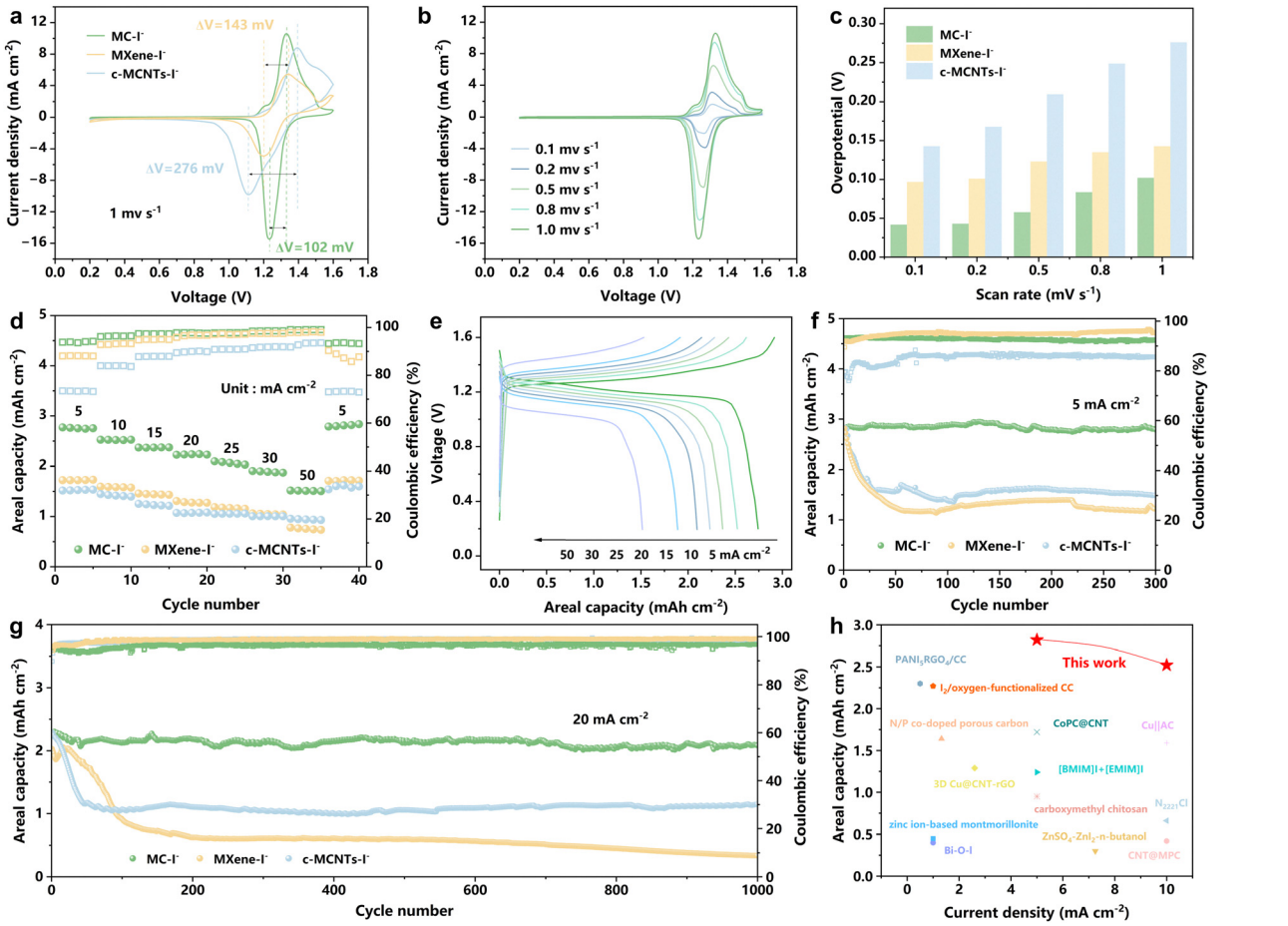

Fig. 4 Electrochemical performance of the MC-I^- cathode. (a) CV curves of the MC-I^-, MXene-I^-, and c-MCNTs-I^- cathodes at a scan rate of 1 mV s^{-1}. (b) CV curves of the MC-I^- cathode at different scan rates. (c) Trend diagram of the polarization overpotentials of the MC-I^-, MXene-I^-, and c-MCNTs-I^- batteries at different scan rates. (d) Rate performances of the MC-I^-, MXene-I^-, and c-MCNTs-I^- cathodes. (e) The GCD curves of the MC-I^- cathode at various rates. (f) Cyclability of the MC-I^-, MXene-I^-, and c-MCNTs-I^- cathodes at 5 mA cm^{-2}. (g) Long-term cycling stability of the MC-I^-, MXene-I^-, and c-MCNTs-I^- cathodes at 20 mA cm^{-2}. (h) Comparison of current density and areal specific capacity of this work to iodine cathodes reported in the literature.

MXene-I^- and c-MCNTs-I^- batteries (Fig. 4a), suggesting that the combination of MXene and c-MCNTs enhances the redox kinetics of the Zn–I_2 battery. The faster I_2/I^- conversion kinetics of the battery using the MC-I^- cathode are further validated using its smaller oxidation and reduction Tafel slopes compared to the batteries with the MXene-I^- and c-MCNTs-I^- cathodes (Fig. S9).[46,47] Electrochemical impedance spectroscopy (EIS) curves also confirm the fast kinetics. Typically, the charge transfer kinetics at the electrode–electrolyte interface play a pivotal role in determining redox kinetics. Fig. S10 shows the EIS profiles of the Zn–I_2 batteries with varying cathodes at the onset potential, which marks the commencement of iodine reduction. The battery incorporating the MC-I^- cathode demonstrates a significantly lower interfacial charge transfer resistance (R_{ct}) (1.26 Ω) compared to those with the MXene-I^- and c-MCNTs-I^- cathodes. The reduced R_{ct} of the MC-I^- cathode suggests faster reaction kinetics during the electrocatalytic iodine conversion process.[48]

Then the CV curves of MC-I^- recorded at various scan rates demonstrate stable redox chemistry (Fig. 4b). As the scan rate increases from 0.1 to 1.0 mV s^{-1}, the shapes of the CV curves remain consistent, and the redox peak pairs remain distinct. To further understand the charge storage mechanism, the non-diffusion limited and diffusion contributions are calculated. The non-diffusion limited contribution can be estimated using the following equation:

$$i(V) = k_1 v + k_2 v^{1/2}$$

where $k_1 v$ represents the non-diffusion limited effects and $k_2 v^{1/2}$ represents the diffusion-controlled contribution.[49] The contribution ratio of the non-diffusion limited process increases as the scan rate rises (Fig. S11), reaching 95.7% at 1.0 mV s^{-1} (Fig. S12), highlighting the high-power capability of MC-I^- due to its micropores, which facilitate efficient Zn^{2+} ion diffusion. The CV curves for batteries with the MXene-I^- and c-MCNTs-I^- cathodes at a scan rate ranging from 0.1 to 1 mV s^{-1} are also collected (Fig. S13 and S14). Fig. 4c presents the trend of the polarization overpotential values relative to the scan rate. As the scan rate increases, the difference in the polarization overpotential gap between the three batteries gradually increases.[50]

This suggests that the battery with the MC-I^- composite cathode exhibits better kinetic performance, faster conversion reactions, and a more stable process.

The following constant current charge–discharge (GCD) tests demonstrate the excellent electrochemical performance of the MC-I^- cathode. Fig. 4d presents the rate capability of the three samples. Within the current density range of 5, 10, 15, 20, 25, 30, and 50 mA cm^{-2}, the discharge specific capacity of the MC-I^- battery is significantly higher than that of the MXene-I^- and c-MCNTs-I^- batteries. Specifically, as shown in Fig. S15, the areal capacity of the high-loading MC-I^- battery is approximately 2.82 mAh cm^{-2}, which is close to the typical value of commercial lithium-ion batteries (3.0 mAh cm^{-2}), about 1.64 times that of the MXene-I^- battery (approximately 1.72 mAh cm^{-2}), and approximately 1.86 times that of the c-MCNTs-I^- battery (approximately 1.52 mAh cm^{-2}). Moreover, the GCD curve corresponding to the MC-I^- cathode in Fig. 4e exhibits a flat discharge plateau even at 50 mA cm^{-2}, and the discharge specific capacity of the MC-I^- battery remains at approximately 1.52 mAh cm^{-2}, which significantly differs from previously reported Zn–I_2 batteries with limited kinetics at high scan rates. After composite preparation, the rapid iodine conversion reaction kinetics enhance the I_2/I^- conversion activity of the MC-I^- composite cathode, thereby improving its specific capacity and rate performance.

Fig. 4f shows the cycling performance of the Zn–I_2 battery using MC-I^-, MXene-I^-, and c-MCNTs-I^- cathodes at 5 mA cm^{-2}. The MC-I^- battery exhibits stable cycling performance at a current density of 5 mA cm^{-2}, retaining 99.04% of its initial capacity after 300 cycles. In contrast, the specific capacities of the MXene-I^- and c-MCNTs-I^- batteries gradually decrease after cycling begins at 5 mA cm^{-2}, dropping to 1.22 mAh cm^{-2} and 1.49 mAh cm^{-2}, respectively, after 300 cycles, with capacity retention rates of only 43.22% and 52.49% (Fig. 4f). Additionally, coulombic efficiency (CE) is a key parameter for evaluating the multi-iodide ion shuttling effect and electrochemical reversibility of the Zn–I_2 battery. As shown in Fig. 4e, the average CE of the MC-I^- battery at 5 mA cm^{-2} after 300 cycles is 93.3%. When the current density is increased to 20 mA cm^{-2}, the average CE of the MC-I^- battery further increases to 96.6%.

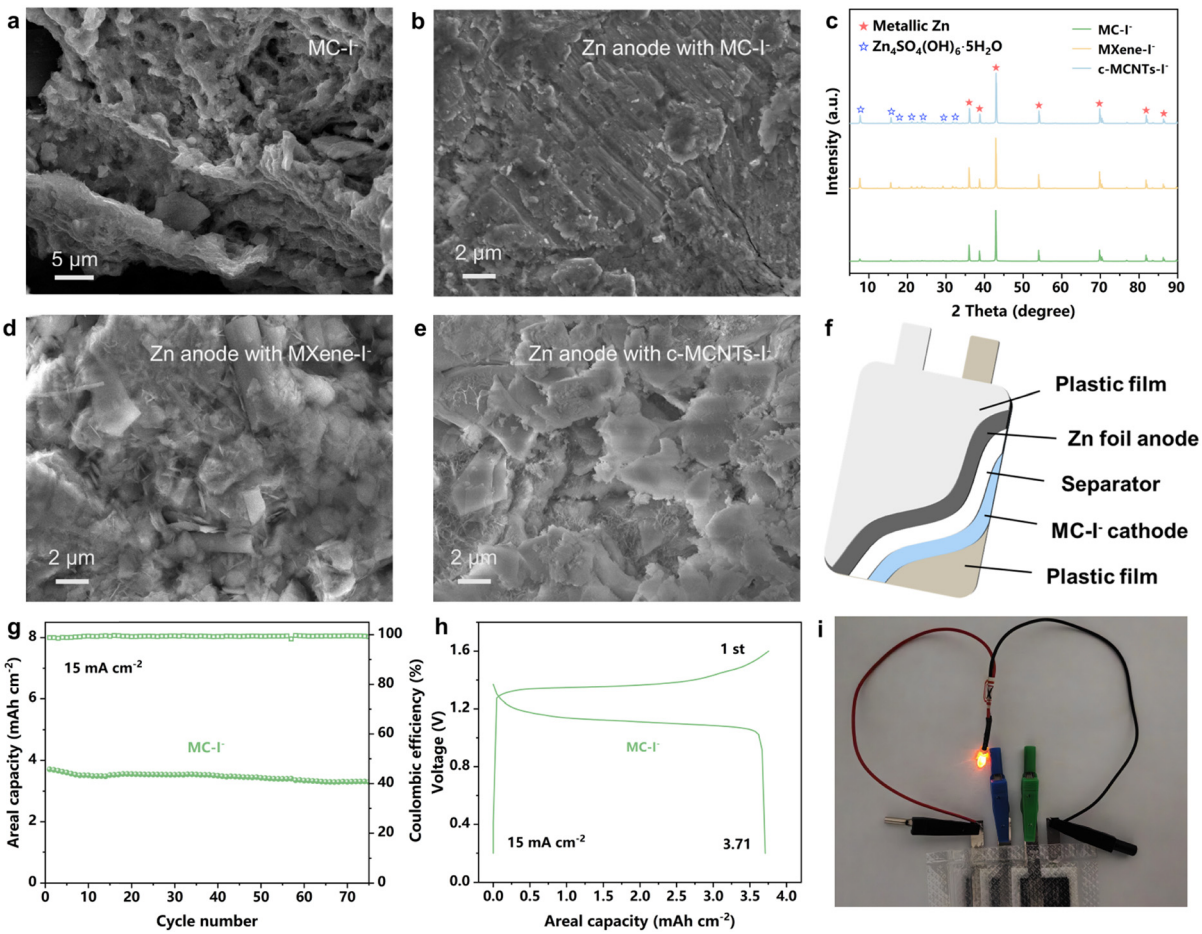

Fig. 5 Mechanism of the durable redox chemistry and pouch-type Zn–I_2 cell with the high iodine-loaded MC-I^- cathode. (a) SEM image of the MC-I^- cathode after the cycling test. (b) SEM image of the cycled Zn metal anodes in the batteries with the MC-I^- cathode. (c) XRD profiles of the cycled Zn metal anodes with the MC-I^-, MXene-I^-, and c-MCNTs-I^- cathodes. (d) and (e) SEM images of the cycled Zn metal anodes in the batteries with the MXene-I^- cathode and the c-MCNTs-I^- cathode. (f) Schematic illustration, (g) cyclability, and (h) the GCD curve of the pouch-type Zn–I_2 battery using the MC-I^- cathode. (i) Digital photograph of three tandem cells used to power a light bulb.

Zn–I_2 batteries with MC-I^- cathodes exhibit better long-term cycling stability compared to those with MXene-I^- and c-MCNTs-I^- cathodes. As shown in Fig. 4g, the MC-I^- battery operates continuously at 20 mA cm^{-2}, with an initial discharge capacity of 2.28 mAh cm^{-2}. It maintains a high capacity retention rate of 91.3% after 1000 cycles (Fig. 4g). Notably, the charge–discharge platform of the MC-I^- battery at the 1000th cycle is very close to that at the first cycle (Fig. S16). In contrast, the cycling progresses, and the charge–discharge platforms are significantly shortened after 1000 cycles (Fig. S17). Similar to the cycling tests at 5 mA cm^{-2}, the rapid capacity decline at 20 mA cm^{-2} is attributed to the pronounced polyiodides shuttle effect. Fig. 4h compares the current Zn–I_2 battery based on a high-loading MC-I^- cathode with previously reported Zn–I_2 batteries in terms of areal capacity.[23,44,51–61] At different current densities, the MC-I^- battery demonstrates superior areal capacity.

The cycled high iodine-loaded MC-I^- cathodes and Zn metal anodes are characterized in detail by using SEM and XRD techniques. The SEM observation (Fig. 5a) reveals that the microstructure of the MC-I^- cathode does not stack significantly after cycling. A hybrid network of MXene and c-MCNTs remains uniformly distributed on the surface of the cycled MC-I^- cathode. In contrast, the MXene-I^- and c-MCNTs-I^- cathodes exhibit significant stacking after cycling (Fig. S18). Fig. 5b, d and e show SEM observations of the cycled Zn metal anodes in the three batteries with different cathodes. The Zn anode cycled with the MC-I^- cathode maintains a smooth and flat surface, while the Zn anodes paired with MXene-I^- and c-MCNTs-I^- cathodes exhibit uneven deposition and the formation of zinc sulfate byproducts. This discrepancy is attributed to the limited ability of MXene-I^- and c-MCNTs-I^- cathodes to anchor polyiodides, leading to the shuttle effect and thus shortening the cycling life of ZnI_2 batteries.[62] In contrast, the integrated composite network structure formed by MXene and c-MCNTs in the MC-I^- cathode effectively restricts the free migration of polyiodides, alleviating the shuttle effect and reducing zinc anode corrosion and byproduct formation.

X-ray diffraction (XRD) analysis further reveals the composition evolution of the cycling zinc anode. As shown in Fig. 5c, in the cycling zinc anode paired with MXene-I^- and c-MCNTs-I^- cathodes, the signal corresponding to basic zinc sulfate ($Zn_4SO_4(OH)_6{\cdot}5H_2O$) is significant and strong,[63] indicating that during the cycling process of the zinc–iodine battery, a large amount of polyiodides is generated. These polyiodides migrate to the zinc anode through the shuttle effect and undergo redox reactions with metallic zinc. This not only leads to the loss of iodine species but also generates hydrated basic zinc sulfate byproducts at or near the anode surface, causing irreversible zinc loss and severely affecting the cycling stability of the ZnI_2 battery, resulting in a rapid capacity decay in batteries with MXene-I^- and c-MCNTs-I^- cathodes. In contrast, in the battery with the MC-I^- cathode under the same cycling conditions, the zinc anode mainly exhibits crystalline zinc metal diffraction peaks, with only trace amounts of basic zinc sulfate signals detected. This indicates that the battery does not produce significant shuttle effects during cycling, and its stability is significantly improved.[22] The XRD analysis further confirms that the MC composite structure plays a crucial role in preventing the polyiodide shuttle, effectively reducing the formation of zinc sulfate byproducts at the zinc anode surface.

The promising performance of Zn/MC-I^- coin cells has motivated us to further investigate the performance in pouch cells, which can be facilely assembled in ambient air without complicated procedures. Fig. 5f schematically illustrates the typical configuration of the pouch cell, and the actual cell is displayed in Fig. S19. Fig. 5h presents the GCD curve of the pouch cell with the MC-I^- cathode, where the battery has an N/P ratio of 3.7 and an E/C ratio of 12.5, achieving a capacity of 3.71 mAh cm^{-2} at a current density of 15 mA cm^{-2}. Fig. 5g shows the cycling performance of the MC-I^- cathode pouch cell at 15 mA cm^{-2}, with a capacity retention of 86.2% after 75 cycles, an average capacity loss of approximately 1.8% per cycle, and a coulombic efficiency of about 99.4%. Finally, to confirm the potential applications of our battery in a real-life scenario, three tandem pouch cells can be employed to power a light bulb (Fig. 5i), evidencing the excellent device scalability.

3. Conclusions

In summary, we developed a high iodine-loaded (MC-I^-) composite cathode for stable aqueous Zn–I_2 batteries. The MC-I^- composite cathode presented an iodine loading as high as 33.27 mg cm^{-2} and achieved a high areal capacity of 2.82 mAh cm^{-2} with 99.04% capacity retention after 300 cycles at a current density of 5 mA cm^{-2} ($\approx$0.15C). Systematic experimental characterization revealed the mechanism by which the $Ti_3C_2T_x$ MXene and c-MCNT composite exerts its regulatory effect. Specifically, the Ti metal centers within the MXene acted as active sites, forming robust chemical adsorption with polyiodide anions. This anchored polyiodides to the cathode and inhibited their shuttling to the anode. Concurrently, the carboxyl groups on c-MCNTs were replaced by I^-, forming strong interactions that anchor the iodine source at the cathode, effectively suppressing the shuttling effect. Furthermore, the microporous structure in the composite material restricted iodine species while ensuring Zn^{2+} diffusion. It is expected that the complementary chemical adsorption strategy proposed in this study opens new avenues for exploring the design of high-loading cathodes.

Author contributions

Aidi Fu.: methodology, conceptualization, investigation, formal analysis, data curation, and writing of original draft. Guohao Li: investigation and visualization. Yingxinjie Wang: investigation and visualization. Jie Wang: investigation and visualization. Jiale Fan: investigation and visualization. Jiamin Liu: investigation and visualization. N. Z.: project administration, funding acquisition, validation, supervision, and review and editing.

X. X.: project administration, funding acquisition, validation, supervision, and review and editing.

Conflicts of interest

There are no conflicts to declare.

Data availability

Supplementary data associated with this article are available in the supplementary information (SI). Supplementary information is available. Supplementary information includes experimental section and additional characterization data, such as SEM, XRD, Raman, contact angle, FTIR, and XPS analyses, as well as electrochemical measurements including Tafel, EIS, CV, and GCD results. See DOI: **https://doi.org/10.1039/d5nh00662g**.

Acknowledgements

This work was supported by the National Natural Science Foundation of China (52272295, 52071137, 51977071, 51802040, and 21802020) and the Science and Technology Innovation Program of Hunan Province (2021RC3066 and 2021RC3067). N. Z. and X. X. also acknowledge the financial support from the Fundamental Research Funds for the Central Universities. The Raman characterization was performed at the Analytical Instrumentation Center of Hunan University.

References

1 J. Ming, J. Guo, C. Xia, W. Wang and H. N. Alshareef, *Mater. Sci. Eng., R*, 2019, **135**, 58–84.
2 N. Guo, W. Huo, X. Dong, Z. Sun, Y. Lu, X. Wu, L. Dai, L. Wang, H. Lin, H. Liu, H. Liang, Z. He and Q. Zhang, *Small Methods*, 2022, **6**, 2200597.
3 J. Wang, Y. Yang, Y. Zhang, Y. Li, R. Sun, Z. Wang and H. Wang, *Energy Storage Mater.*, 2021, **35**, 19–46.
4 L. Yan, S. Zhang, Q. Kang, X. Meng, Z. Li, T. Liu, T. Ma and Z. Lin, *Energy Storage Mater.*, 2023, **54**, 339–365.
5 D. Lin, D. Rao, S. Chiovoloni, S. Wang, J. Q. Lu and Y. Li, *Nano Lett.*, 2021, **21**, 4129–4135.
6 M. Xing, Z. Z. Zhao, Y. J. Zhang, J. W. Zhao, G. L. Cui and J. H. Dai, *Mater. Today Energy*, 2020, **18**, 100534.
7 S.-J. Zhang, J. Hao, H. Li, P.-F. Zhang, Z.-W. Yin, Y.-Y. Li, B. Zhang, Z. Lin and S.-Z. Qiao, *Adv. Mater.*, 2022, **34**, 2201716.
8 D. Lin and Y. Li, *Adv. Mater.*, 2022, **34**, 2108856.
9 X. Yang, H. Fan, F. Hu, S. Chen, K. Yan and L. Ma, *Nano-Micro Lett.*, 2023, **15**, 126.
10 Y. Wang, X. Jin, J. Xiong, Q. Zhu, Q. Li, R. Wang, J. Li, Y. Fan, Y. Zhao and X. Sun, *Adv. Mater.*, 2024, **36**, 2404093.
11 G. Chen, Y. Kang, H. Yang, M. Zhang, J. Yang, Z. Lv, Q. Wu, P. Lin, Y. Yang and J. Zhao, *Adv. Funct. Mater.*, 2023, **33**, 2300656.
12 T. Liu, C. Lei, H. Wang, J. Li, P. Jiang, X. He and X. Liang, *Adv. Mater.*, 2024, **36**, 2405473.
13 X. Li, N. Li, Z. Huang, Z. Chen, G. Liang, Q. Yang, M. Li, Y. Zhao, L. Ma, B. Dong, Q. Huang, J. Fan and C. Zhi, *Adv. Mater.*, 2021, **33**, 2006897.
14 M. Han, D. Chen, Q. Lu and G. Fang, *Small*, 2024, **20**, 2310293.
15 H. Pan, B. Li, D. Mei, Z. Nie, Y. Shao, G. Li, X. S. Li, K. S. Han, K. T. Mueller, V. Sprenkle and J. Liu, *ACS Energy Lett.*, 2017, **2**, 2674–2680.
16 J. Ye, W. Tian, Y. Du and J. Ji, *Adv. Funct. Mater.*, 2025, 2509582.
17 W. Li, P. Hei, Y. Sai, J. Meng, Y. Yu, Y. Song and X.-X. Liu, *Chem. Eng. J.*, 2025, **510**, 161720.
18 G. Li, J. Wang, J. Fan, Y. Wang, C. Chen, N. Zhang and X. Xie, *ACS Nano*, 2025, **19**, 31010–31022.
19 J. Wang, G. Li, G. Xie, Z. Huang, P. Zhang, B. Xu, X. Xie and N. Zhang, *SusMat*, 2024, **4**, e202.
20 G. Li, J. Fan, J. Wang, Y. Wang, C. Chen, H. He, K. Tang, Z. Wu, N. Zhang and X. Xie, *Adv. Funct. Mater.*, 2025, e14630.
21 X. Guo, H. Xu, Y. Tang, Z. Yang, F. Dou, W. Li, Q. Li and H. Pang, *Adv. Mater.*, 2024, **36**, 2408317.
22 D. Li, Y. Zhu, L. Cheng, S. Xie, H. Yu, W. Zhang, Z. Xu, M. Ma and H. Li, *Adv. Energy Mater.*, 2024, 2404426.
23 J. He, H. Hong, S. Hu, X. Zhao, G. Qu, L. Zeng and H. Li, *Nano Energy*, 2024, **119**, 109096.
24 S. Tian, G. Cheng, Z. Tang, F. Sha, Z. Xuan and G. Ding, *Ceram. Int.*, 2020, **46**, 28949–28954.
25 W. Xu, Z. Xu, Y. Liang, L. Liu and W. Weng, *Nanotechnology*, 2021, **32**, 355706.
26 J. Wang, L. Hao, J. Qin, X. Zhang, Y. Cheng, L. Yue, Y. Wang, M. Jiang, Z. Wang and M. Cao, *Energy Storage Mater.*, 2024, **66**, 103209.
27 S. A. Kazemi, S. A. Ogunkunle, O. Allen, W. Wen, A. W.-C. Liew, S. Yin and Y. Wang, *J. Phys. Mater.*, 2023, **6**, 035004.
28 M. M. H. Raza, M. Sadiq, S. Khan, M. Zulfequar, M. Husain, S. Husain and J. Ali, *Diamond Relat. Mater.*, 2020, **110**, 108139.
29 Y. Yoshida, Y. Ishii, N. Kato, C. Li and S. Kawasaki, *J. Phys. Chem. C*, 2016, **120**, 20454–20461.
30 Y. Li, L. Liu, H. Li, F. Cheng and J. Chen, *Chem. Commun.*, 2018, **54**, 6792–6795.
31 L. Zhou, Y. Yang, J. Yang, P. Ye, T. Ali, H. Wang, J. Ning, Y. Zhong and Y. Hu, *Appl. Surf. Sci.*, 2022, **604**, 154526.
32 M. Liu, Q. Chen, X. Cao, D. Tan, J. Ma and J. Zhang, *J. Am. Chem. Soc.*, 2022, **144**, 21683–21691.
33 S. Mallakpour, M. Dinari and V. Behranvand, *J. Mater. Sci.*, 2014, **49**, 7004–7013.
34 S. Goyanes, G. R. Rubiolo, A. Salazar, A. Jimeno, M. A. Corcuera and I. Mondragon, *Diamond Relat. Mater.*, 2007, **16**, 412–417.
35 S. A. Mammadova, A. B. Huseynov and A. O. Israfilov, *Opt. Spectrosc.*, 2018, **125**, 921–927.
36 S. Mishra and N. Sankararamakrishnan, *Environ. Sci. Pollut. Res.*, 2018, **25**, 12686–12701.
37 L. Zhang, J. Gong, H. Guo, J. Huang, S. Chen, J.-F. Gohy, Y. Zhou, J. Hofkens, T. Liu, K. Müllen and F. Lai, *Adv. Mater.*, 2025, e14117.

38 L. Zhang, K. Luo, J. Gong, Y. Zhou, H. Guo, Y. Yu, G. He, J.-F. Gohy, I. P. Parkin, J. Hofkens, Q. He, T. Liu, K. Müllen and F. Lai, *Angew. Chem., Int. Ed.*, 2025, **64**, e202506822.
39 L. Zhang, H. Ding, H. Gao, J. Gong, H. Guo, S. Zhang, Y. Yu, G. He, T. Deng, I. P. Parkin, J. Hofkens, X. Fan, F. Lai and T. Liu, *Energy Environ. Sci.*, 2025, **18**, 2462–2473.
40 L. Yan, T. Liu, X. Zeng, L. Sun, X. Meng, M. Ling, M. Fan and T. Ma, *Carbon*, 2022, **187**, 145–152.
41 H. Tian, T. Gao, X. Li, X. Wang, C. Luo, X. Fan, C. Yang, L. Suo, Z. Ma, W. Han and C. Wang, *Nat. Commun.*, 2017, **8**, 14083.
42 P. Gao, Z. Zhang, L. Feng, Y. Liu, Z. Du and L. Zhang, *Chem. Eng. J.*, 2021, **426**, 130764.
43 C. Sun, X. Shi, Y. Zhang, J. Liang, J. Qu and C. Lai, *ACS Nano*, 2020, **14**, 1176–1184.
44 X. Wang, Y. Sun, Q. Wang, L. Tang, H. Wang, T. Mu, Y. Zhang, X. Zhu and J. Gao, *Adv. Funct. Mater.*, 2025, 2502268.
45 H. Chen, X. Li, K. Fang, H. Wang, J. Ning and Y. Hu, *Adv. Energy Mater.*, 2023, **13**, 2302187.
46 F. Wei, T. Zhang, H. Xu, Y. Peng, H. Guo, Y. Wang, S. Guan, J. Fu, C. Jing, J. Cheng and S. Liu, *Adv. Funct. Mater.*, 2024, **34**, 2310693.
47 F. Yang, J. Long, J. A. Yuwono, H. Fei, Y. Fan, P. Li, J. Zou, J. Hao, S. Liu, G. Liang, Y. Lyu, X. Zheng, S. Zhao, K. Davey and Z. Guo, *Energy Environ. Sci.*, 2023, **16**, 4630–4640.
48 T. Liu, H. Wang, C. Lei, Y. Mao, H. Wang, X. He and X. Liang, *Energy Storage Mater.*, 2022, **53**, 544–551.
49 F. Wang, Z. Liu, C. Yang, H. Zhong, G. Nam, P. Zhang, R. Dong, Y. Wu, J. Cho, J. Zhang and X. Feng, *Adv. Mater.*, 2020, **32**, 1905361.
50 P.-F. Zhang, J.-H. Li, S.-J. Zhang, D.-C. Li, S.-Y. Zeng, S.-L. Xu, Q.-X. Yao, L.-Y. Liu, L. Ding, H.-X. Li, Y.-Y. Hu, J.-T. Li and Y. Zhou, *Adv. Funct. Mater.*, 2024, **34**, 2306359.
51 W. Yan, Y. Liu, J. Qiu, F. Tan, J. Liang, X. Cai, C. Dai, J. Zhao and Z. Lin, *Nat. Commun.*, 2024, **15**, 9702.
52 Y. Hou, L. Wei, N. Sun, D. Yu and G. Zhao, *J. Energy Storage*, 2025, **120**, 116495.
53 X. Wu, W. Wei, X. Yang, L. Yu and X. C. Chen, *Chem. Commun.*, 2025, **61**, 4543–4546.
54 X. Wu, X. Yang, L. Yu and X. Chun Chen, *Chem. Eng. J.*, 2024, **500**, 157437.
55 Q. Jin, S. Gao, Y. Wang and Z. Qin, *ACS Sustainable Chem. Eng.*, 2024, **12**, 16744–16758.
56 H. Xu, W. Gao, H. Dou, X. Zhang and M. Pumera, *Adv. Funct. Mater.*, 2025, **35**, 2414022.
57 L. Zhou, X. Li, H. Chen, H. Zheng, T. Zhang, J. Ning, H. Wang and Y. Hu, *ACS Appl. Mater. Interfaces*, 2024, **16**, 53881–53893.
58 W. Shi, Z. Song, W. Zhang, S. Lian, F. Huang, Q. An and Q. Li, *Energy Environ. Sci.*, 2024, **17**, 7372–7381.
59 M. Cui, H. Zhao, D. Yin, N. Gao, Y. Zhang, L. Zhao, Y. Wei, M. Liu, K. Xi and S. Ding, *Energy Storage Mater.*, 2024, **69**, 103372.
60 H. Xu, R. Zhang, D. Luo, J. Wang, H. Dou, X. Zhang and G. Sun, *ACS Nano*, 2023, **17**, 25291–25300.
61 R. Yi, X. Shi, Y. Tang, Y. Yang, P. Zhou, B. Lu and J. Zhou, *Small Structures*, 2023, **4**, 2300020.
62 Z. Li, X. Wu, X. Yu, S. Zhou, Y. Qiao, H. Zhou and S.-G. Sun, *Nano Lett.*, 2022, **22**, 2538–2546.
63 K. Wang, H. Li, Z. Xu, Y. Liu, M. Ge, H. Wang, H. Zhang, Y. Lu, J. Liu, Y. Zhang, Y. Tang and S. Chen, *Adv. Energy Mater.*, 2024, **14**, 2304110.